

Time-resolved imaging of the reaction coordinate

Richard Mabbs, Kostyantyn Pichugin, and Andrei Sanov^{a)}

Department of Chemistry, University of Arizona, Tucson, Arizona 85721-0041

(Received 26 January 2005; accepted 16 February 2005; published online 2 May 2005)

Time-resolved photoelectron imaging of negative ions is employed to study the dynamics along the reaction coordinate in the photodissociation of IBr^- . The results are discussed in a side-by-side comparison with the dissociation of I_2^- , examined under similar experimental conditions. The I_2^- anion, extensively studied in the past, is used as a reference system for interpreting the IBr^- results. The data provide rigorous dynamical tests of the anion electronic potentials. The evolution of the energetics revealed in the time-resolved (780 nm pump, 390 nm probe) I_2^- and IBr^- photoelectron images is compared to the predictions of classical trajectory calculations, with the time-resolved photoelectron spectra modeled assuming a variety of neutral states accessed in the photodetachment. In light of good overall agreement of the experimental data with the theoretical predictions, the results are used to construct an experimental image of the IBr^- dissociation potential as a function of the reaction coordinate. © 2005 American Institute of Physics. [DOI: 10.1063/1.1887170]

I. INTRODUCTION

The dynamics of molecular systems on excited potential energy surfaces are most effectively unraveled via direct time-resolved measurements. With the development of new advanced techniques of femtosecond spectroscopy,¹⁻⁴ our view of chemical reactions has evolved from the popular emphasis on atomic rearrangements to the explicit accent on the more fundamental dynamics involving transformations of the electronic structure.^{5,6} Conceptually, chemical reactions can be viewed in terms of atomic motions on the electronic potential energy landscapes or as the structural and energetic changes involving the molecular orbitals. Both points of view are closely interrelated, yet it is the electrons that control chemical bonding and ultimately determine the reaction's outcome.

In the field of negative-ion spectroscopy, a revolutionary breakthrough in the observation of dynamics from the electronic perspective was accomplished with the Neumark group's introduction of femtosecond photoelectron spectroscopy.⁵ The technique, based on a combination of time-resolved pump-probe spectroscopy and anion photoelectron spectroscopy⁷ was successfully applied to investigate the intricate details of the photodissociation of I_2^- .⁸⁻¹⁰ Neumark's original experiments showed that following the excitation with a 780 nm pump pulse, the dissociation is essentially complete within the first 320 fs, yet the interaction between the separating fragments lingers for a further 400 fs.^{8,10} These exit-channel dynamics have been attributed to the polarization-induced attraction between the I^- anion and neutral I atom, which corresponds to a shallow well on the long-range part of the $\text{I}+\text{I}^-$ dissociation potential.

A further advance, which greatly enhanced the capabilities of time-resolved photoelectron spectroscopy, came very recently with the introduction of the photoelectron imaging approach to negative-ion photodetachment. Imaging¹¹ has

proved powerful in many facets of gas-phase dynamics^{12,13} and its application to time-resolved studies, as a means of studying electronic-structure evolution in reactions, is particularly rewarding.¹⁴⁻²⁷

Following the successful application of photoelectron imaging to molecular and cluster anions,²⁸⁻³⁵ Neumark's group applied the imaging approach to time-resolved photoelectron spectroscopy of negative ions.^{26,27} Revisiting the photodissociation of I_2^- , they examined the formation of I^- in the diatomic-anion dissociation with an additional emphasis on the time-dependent photoelectron angular distributions.²⁷ Their success was furthered by our group with the first application of time-resolved photoelectron imaging to a mixed trihalide anion.³⁶ Focusing on the I^- channel in the photodissociation of I_2Br^- , we examined the emergence of the fragment-anion electronic identity and the effect of exit-channel interactions on the electronic structure and photodetachment dynamics.

The simultaneous observation of the time-resolved and mutually dependent photoelectron angular and energy distributions is of great benefit to studies of electronic-structural effects in chemical reactions. The time-dependent photoelectron angular distributions reflect the transformations of the molecular orbitals, while the time-resolved energy spectra shed light on the details of the reactive potential energy surface and evolution of the molecular structure in real time, along the reaction coordinate.

The primary goal of this paper is to demonstrate the application of time-resolved photoelectron imaging, supported by theoretical modeling, for "imaging" the reaction coordinate in IBr^- photodissociation, thus providing a rigorous dynamical test of the recently calculated potentials.^{37,38} Although modern theory is capable of tackling, to a degree, the more challenging polyatomic systems, diatomic molecules afford the most straightforward tests of structure and dynamics. The present experiments on IBr^- are part of a side-by-side comparative study of the photodissociation dy-

^{a)}Electronic mail: sanov@u.arizona.edu

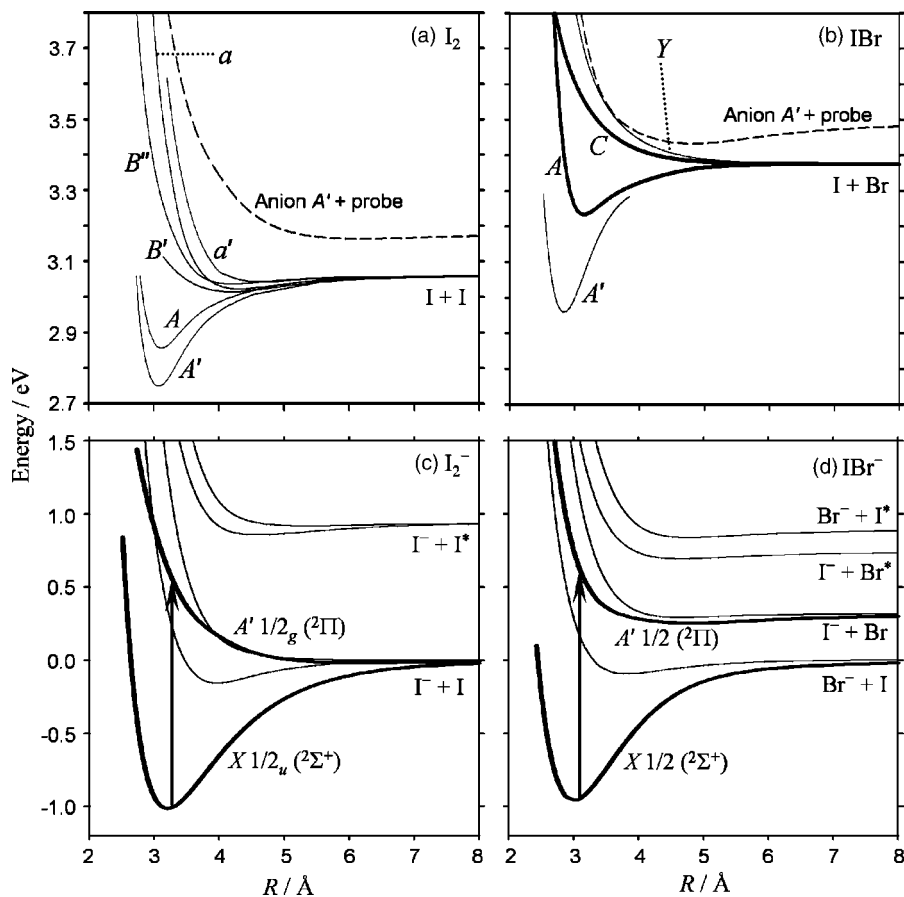


FIG. 1. Potential energy curves for the relevant electronic states of (a) I_2 , (b) IBr and the corresponding anions: (c) I_2^- and (d) IBr^- . The potential curves corresponding to the neutral states of I_2 and IBr are obtained from Refs. 30, 31, 68, 69, 73, 74, 78, 79, and 79–81, respectively. The I_2^- potentials are from the scaled calculations in Refs. 58 and 59, with the exception of the X and A' states, which are experimentally determined in Refs. 3, 4, 10, and 57. The IBr^- curves are from Refs. 37 and 38. The vertical arrows in (c) and (d) represent the pump transition accessing the A' states of the respective anions. The dashed curves in (a) and (b) represent the A' anion potentials projected onto the respective neutral manifolds by the addition of the probe photon energy. Further details are given in the text.

dynamics of the I_2^- and IBr^- anions. The former has been studied extensively, both in isolation and in solvated environments.^{8–10,39–55} Of particular note are the aforementioned experiments by the Neumark group.^{8,10,56} The I_2^- anion, therefore, provides an excellent reference system for interpreting the results for IBr^- , for which few theoretical and experimental gas-phase studies are available.³⁷

Figure 1 displays the relevant electronic potential energy curves for the I_2^- and IBr^- anions, as well as the corresponding neutral molecules. The energy scale for the neutrals in Figs. 1(a) and 1(b) is not the same as for the anions in Figs. 1(c) and 1(d). Considering the anions first, the ground X and excited A' state potentials of I_2^- , represented by bold lines in Fig. 1(c), are taken from the experimental work of Zanni *et al.*,^{3,4,10,57} while the other four I_2^- state potentials are from the scaled *ab initio* calculations of Faeder and Parson.^{58,59} The IBr^- potentials in Fig. 1(d) are the unmodified results of the *ab initio* calculations by Thompson and Parson³⁸ for the six lowest states of the anion,³⁷ with the bold curves again representing the ground X and excited A' states.

The vertical arrows in Figs. 1(c) and 1(d) represent the 780 nm pump photon energy used in the experiments described in this paper. The corresponding excitations access primarily the respective A' states, namely the $A' 1/2(^2\Pi)$ state of IBr^- and the $A' 1/2_g(^2\Pi)$ state of I_2^- , where the states are labeled according to Hund's case (c), with the Hund's case (a) notation given in parentheses. Spin-orbit interaction plays an important role in both anions. At R_e , the ground electronic state equilibrium bond distance, the basic

Hund's case (a) character is retained, but spin-orbit mixing of the states becomes increasingly important with increasing internuclear separation.⁶⁰

In I_2^- , the prompt 780 nm dissociation on the A' electronic state leads to the lowest-energy product channel, $I^- + I(^2P_{3/2})$, with a 0.6 eV fragment kinetic energy release. The lowest optically bright excited electronic state of IBr^- correlates to the second lowest, $I^- + Br(^2P_{3/2})$ channel. In this case, at 780 nm, the kinetic energy release is 0.2 eV. In this work, the dynamics for each case are probed through 390 nm electron detachment with delayed probe laser pulses, accessing the respective manifolds of I_2 and IBr neutral states shown in Figs. 1(a) and 1(b). Only the pertinent neutral states accessible by photodetachment from the respective A' anion states at the probe photon energy employed here are included in Figs. 1(a) and 1(b).

An important distinction between the excited-state interactions in IBr^- and I_2^- is the existence of an attractive well on the A' potential in IBr^- . To highlight this well, the dashed curve in Fig. 1(b) represents the $IBr^- A'$ state potential offset by 3.18 eV, the probe photon energy, projecting this anion state on the corresponding neutral manifold. In comparison, the analogous A' potential well is nearly absent in I_2^- , as indicated by a similar dashed curve in Fig. 1(a).

Nonetheless, the shallow, 17 meV deep, well on the A' potential in I_2^- was observed by Zanni *et al.*¹⁰ It is attributed to the weak polarization-induced attraction between the separating I^- anion and neutral I atom. In contrast, the more pronounced well on the A' potential in IBr^- has never been

observed experimentally. Fundamentally, in IBr^- this well is due to charge-switching in the heteronuclear system and can be seen as arising from the different electron affinities of Br and I (3.36 and 3.06 eV, respectively).⁶¹ Hence, as the molecular anion dissociates on the A' IBr^- state, the excess electron is shifted from a delocalized molecular orbital into an atomic orbital of the less energetically favorable I^- fragment, causing an attractive interaction between the separating I^- and Br fragments.

The electronic-state potentials for IBr^- were developed only recently^{37,38} and to our knowledge have yet to be subjected to dynamical testing. This paper reports the first application of femtosecond time-resolved photoelectron imaging to the dissociation of IBr^- . The experimental approach and simulation methods used in this work are tested on the analogous (but better characterized) I_2^- anion, showing an agreement with previous studies of this system. The time-resolved photoelectron imaging investigation of IBr^- dissociation is then presented and used to generate an experimental portrait of the anion potential for comparison with the *ab initio* results.

II. EXPERIMENTAL APPARATUS

The apparatus used in this study employs pulsed negative-ion generation and mass-analysis techniques,^{62,63} combined with a velocity-mapped,⁶⁴ imaging¹¹ scheme for detection of photoelectrons. The experimental arrangement is that previously used in both “static” and time-domain detachment studies.^{34,36} Here we present only the details pertinent to this new study.

To generate I_2^- and IBr^- , the ambient vapor pressure of IBr seeded in Ar is expanded through a pulsed nozzle (General Valve Series 9 with a Kel-F poppet) operated at a repetition rate of 70 Hz into a high-vacuum chamber with a base pressure of 10^{-6} Torr (rising to 3×10^{-5} Torr when the pulsed valve is operated). The supersonic expansion is crossed with a 1 keV electron beam and the resulting anions are pulse-extracted into a 2-m-long Wiley-McLaren time-of-flight mass spectrometer.⁶⁵ After the ion beam is accelerated to about 2.5 keV and focused using an Einzel lens, it enters the detection region with a typical base pressure of $3\text{--}5 \times 10^{-9}$ Torr. The ions are detected mass-selectively using a dual microchannel plate (MCP) detector (Burle, Inc.) at the end of the flight tube.

The mass-selected I_2^- and I^{79}Br^- anions are photolyzed by the 780 nm pump pulses and the evolving electronic structure is probed via photodetachment with delayed 390 nm probe laser pulses. The regeneratively amplified Ti:sapphire laser system (Spectra Physics, Inc.) produces 1 mJ, 100 fs pulses at 780 nm. Half of the fundamental output is used as the pump beam, while the other half is channeled through the 100- μm -thick BBO crystal of a femtosecond harmonics generator (Super Optonics, Inc.), producing 100 μJ pulses with a bandwidth of 5 nm at 390 nm. The spectral profile of the UV output is monitored using a fiberoptic spectrometer (Ocean Optics, Inc.). The 390 nm probe beam passes through a motorized translation stage (Newport ESP300 Universal Motion Controller) to enable controlled temporal separation

of the pump and probe pulses. The pump and probe beam paths are combined before entering the reaction chamber using a dichroic beam splitter. The polarization vectors of the two beams are parallel to each other and to the ion beam axis. Both laser beams are mildly focused using a 1 m focal length lens positioned approximately 45 cm before the intersection with the ion beam.

The position of zero delay is determined by overlapping the pump and probe pulses in a BBO crystal. By monitoring the third harmonic generation as a function of delay, the cross-correlation before the vacuum chamber entrance window is measured to be about 300 fs (full width at half-maximum). This defines the approximate time-resolution of the experiment. The passage of the beams through the chamber window introduces an additional (dispersion induced) pump-probe delay, which is accounted for by reference to the I_2^- experiments of the Neumark group at the same pump wavelength.^{8,10,56}

The photodetached electrons are detected using velocity-map⁶⁴ imaging¹¹ in the direction perpendicular to the ion and laser beams. A 40-mm-diam MCP detector with a P47 phosphor screen (Burle Inc.) is mounted at the end of an internally μ -metal shielded electron flight tube. Images are obtained from the phosphor screen using a CCD camera (Roper Scientific Inc.). To suppress background signals, the potential difference across the two MCPs is only pulsed up to 1.8 kV for a 200-ns-wide collection window, timed to coincide with the arrival of the photoelectrons. For the rest of each experimental cycle, the dual-MCP potential difference is maintained at 1.0–1.2 kV, which is not enough to produce a detectable signal.

Extraneous pump or probe photon detachment signals are removed using computer-controlled shutters in the pump and probe beam paths and the data acquisition and correction algorithm described previously.³⁶ Each of the images presented in this work represents the result of $\sim 10^5\text{--}10^6$ experimental cycles.

III. RESULTS

Figure 2 shows representative photoelectron images obtained at selected pump-probe delays. The I_2^- and IBr^- images were recorded under similar experimental conditions and are shown alongside each other. The “ $t=\infty$ ” image at the top of Fig. 2 was recorded in the one-photon detachment of I^- using only the 390 nm (probe) radiation. The image is shown here for reference, as it represents the asymptotic limit of both the IBr^- and I_2^- dissociation channels yielding iodide anion fragments.

All images in Fig. 2 were recorded with linearly polarized pump and probe laser beams, the polarization direction being vertical in the plane of the images. The cylindrical symmetry imposed by this polarization geometry enables the complete reconstruction of the photoelectron velocity and angular distributions by means of inverse Abel transformation.¹² The Abel inversion is performed with the Basis Set Expansion (BASEX) program developed by Reisler and co-workers.⁶⁶

The ensuing discussion focuses on the time-dependent

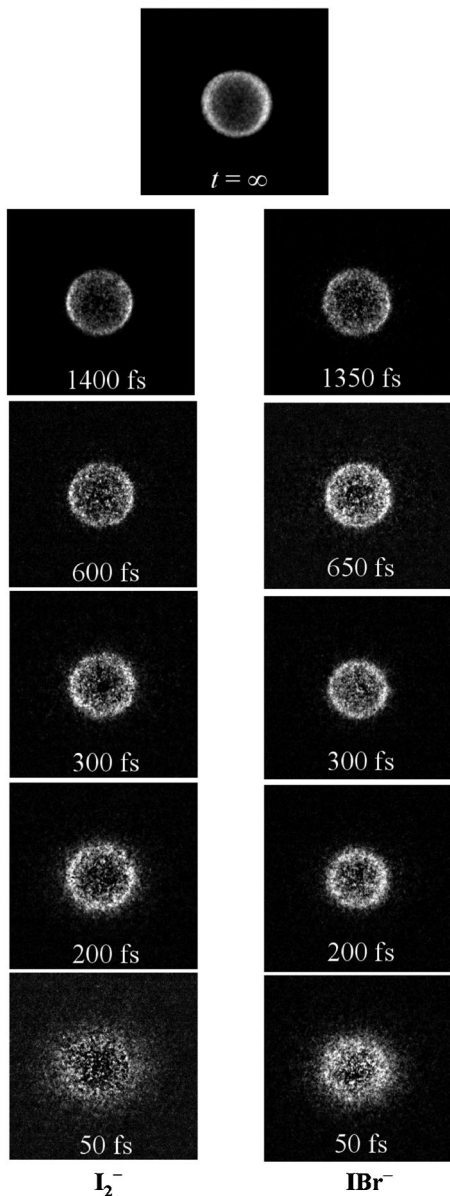


FIG. 2. Representative time-resolved raw photoelectron images recorded at selected pump-probe delays in the 780 nm pump-390 nm probe experiments on I_2^- (left) and IBr^- (right). The pump and probe polarization directions are vertical in the plane. The images are shown on arbitrary relative intensity scales.

photoelectron spectra, shown in Figs. 3(a) and 3(b) for the dissociation of I_2^- and IBr^- , respectively. The spectra, extracted from the images in Fig. 2 using the BASEX algorithm, quantify the time-dependent changes in the energetics and reflect the evolution of the electronic structure of the dissociating diatomic anions. In both IBr^- and I_2^- , a single evolving band is observed, which asymptotically (at long delays) corresponds to detachment from the final I^- fragment. This conclusion is consistent with the energetics of the band, whose position at long pump-probe delays is in agreement with the electron affinity of atomic iodine (3.06 eV).⁶¹ The asymptotic width of the band reflects the experimental resolution in the relevant energy range, i.e., ~ 0.05 eV full width at half-maximum.

Examining first the time-dependent I_2^- spectra in Fig.

3(a), we note a very slight shift in the position of the band toward smaller eKE during the early stages of the dissociation, followed by a reverse shift toward the asymptotic value of eKE=0.12 eV at longer delays. This transient dip in eKE, first observed by Zanni *et al.* using 260 nm probe pulses, is attributed to a shallow (0.017 ± 0.010 eV) well on the $A' I_2^-$ potential with a minimum at $R=6.2$ Å.¹⁰ The well arises from a long-range polarization-induced attraction between the fragments.

Using the I_2^- spectra as a reference for interpreting the IBr^- results, we note that in the latter case the evolving detachment band exhibits a much more pronounced dip in eKE. The distinction between the IBr^- and I_2^- data is best seen with these results presented as the two-dimensional time-energy plots shown in Fig. 4. Figures 4(a) and 4(b) reflect the evolution of the dissociative wave packets for I_2^- and IBr^- , respectively, within the relevant eKE range of 0–0.3 eV. The curves plotted over the contour plots in Fig. 4 represent the classical trajectory simulations described in Sec. IV.

IV. MODELING AND DISCUSSION

Both I_2^- and IBr^- dissociations at 780 nm produce the same ionic fragment, the iodide anion. The experiments by Lineberger and co-workers at a similar wavelength indicate the absence of Br^- fragments.³⁷ It is also important that the probe photons used here do not have sufficient energy to detach an electron from Br^- . Hence, the IBr^- pump-probe experiment is inherently sensitive only to the anion states that correlate to I^- formation.

Knowing the electronic state potentials for IBr^- and I_2^- , it is possible to model the direct dissociation dynamics using a quantum-mechanical¹⁰ or classical approach. The goals of this work are achieved within the classical framework, which confines the quantum-mechanical aspects of the problem to the electronic-state potentials.

We obtain the I_2^- and IBr^- dissociation trajectories by solving Newton's second-law equation,

$$\mu \frac{d^2 R}{dt^2} = - \frac{dV_{an}(R)}{dR}, \quad (1)$$

where R is the internuclear distance, μ is the reduced mass of the diatomic anion, and $V_{an}(R)$ is the potential energy curve for the anion state on which the dissociation takes place. The classical trajectories $R(t)$ obtained by integrating Eq. (1) reflect the evolution of the expectation value of R for the corresponding quantum wavepackets.

Within the classical framework, the time-resolved photoelectron spectra reflect the evolving difference between the neutral and anion electronic potentials, according to

$$eKE(R) = [h\nu + V_{an}(R)] - V_{nu}(R), \quad (2)$$

where $V_{an}(R)$ is the anion dissociation potential accessed by the pump laser pulse and $V_{nu}(R)$ is the electronic potential of the neutral state accessed in the photodetachment by the probe pulse. Therefore, classically, every point on the dissociation trajectory $R(t)$ corresponds to a specific value of the photoelectron kinetic energy.

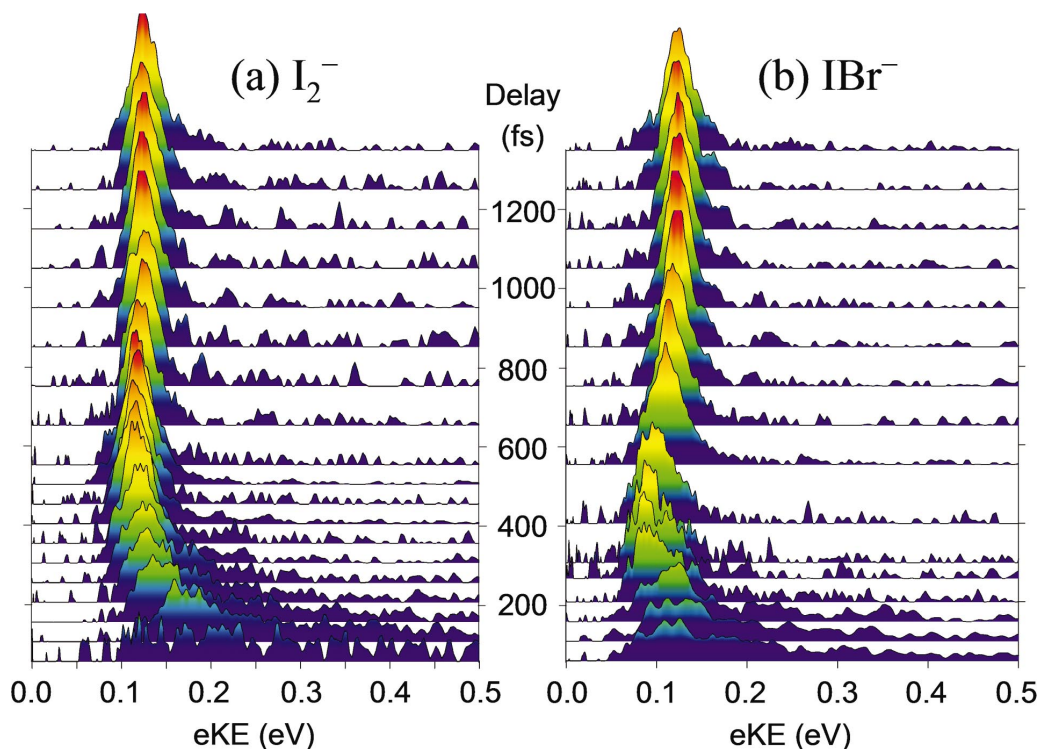


FIG. 3. (Color) Time-resolved photoelectron spectra obtained in the dissociation of (a) I_2^- and (b) IBr^- using a 780 nm pump, while detaching the electrons with 390 nm probe pulses. The spectra are obtained from photoelectron images, a selection of which is shown in Fig. 2.

Since the long-range interactions between neutral fragments are much weaker than the ion–neutral interactions in the dissociating anions, the neutral potential can be seen as essentially flat in the long range. Therefore, at sufficiently long delays, the evolution of the pump–probe spectra in Figs. 3 and 4 reflects the shape of the long-range anion potential on which the dissociation takes place. At shorter internuclear

separations, the interactions in the neutral systems are important as well and the analysis of the short-delay spectra must include the details of the neutral electronic potential.

In the following, we first describe the application of the model given by Eqs. (1) and (2) to the dissociation of I_2^- (Sec. IV A). This serves to illustrate that the experimental spectra obtained in the present work are in a good agreement

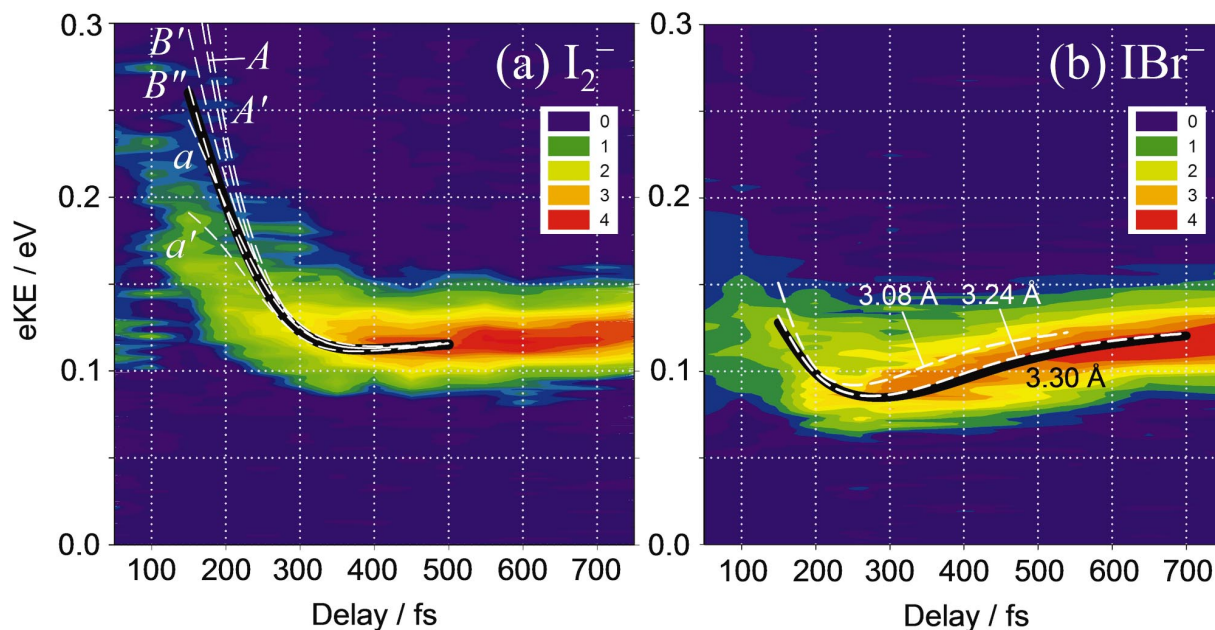


FIG. 4. (Color) Time–energy contour plots of the time-resolved photoelectron spectra shown in Fig. 3 in the range of 50–750 fs and 0.0–0.3 eV for (a) I_2^- and (b) IBr^- . In (a), the dashed white curves represent trajectory simulations with detachment via the labeled neutral states. The solid black line represents a mean of the individual detachment channels, calculated as described in the text. In (b), the lines represent trajectories corresponding to the different values of R_0 indicated. The “best fit” (as determined by inspection), corresponding to $R_0 = 3.30$ Å, is indicated by the solid black line.

with the A' anion potential determined by Zanni *et al.*¹⁰ Subsequently, in Sec. IV B, the same approach is applied to the dissociation of IBr^- , to test the theoretical A' potential³⁷ for this system. Considering that this work is the first dynamical test of the calculated IBr^- potential, in Sec. IV C we take the experimental results for this system a step further and use the data, in conjunction with theoretical modeling, to generate an experiment-based “image” of the dissociation potential.

A. Modeling I_2^- dissociation

The I_2^- dissociation trajectory was calculated by substituting the $A' 1/2_g(^2\Pi)$ state potential of I_2^- determined by Zanni *et al.*^{10,57} for $V_{\text{an}}(R)$ in Eq. (1). The equation of motion was integrated on a time-grid with a constant 1 fs step size. Rather than launching the A' trajectory from the ground electronic state equilibrium bond length ($R_e=3.24 \text{ \AA}$),^{3,4} R_0 was chosen as a point on the A' anion potential lying above the X state equilibrium by the value of the pump photon energy, $h\nu=1.59 \text{ eV}$. Based on the experimentally determined $\text{I}_2^- X$ and A' potentials,^{3,4,10,57} this corresponds to $R_0=3.25 \text{ \AA}$, compared to the I_2^- ground-state equilibrium bond length $R_e=3.24 \text{ \AA}$.^{3,4} Although a minor discrepancy does exist, launching a classical trajectory on the A' potential with R_0 equal to the Franck–Condon bond length requires more energy than is supplied by the pump photon. The initial velocity was assumed to be zero.

Considering the photodetachment (probe) step, there are ten neutral electronic states of I_2 that correlate asymptotically to the $\text{I}(^2P_{3/2})+\text{I}(^2P_{3/2})$ dissociation limit.⁶⁷ Of these, seven have been characterized experimentally,^{30,31,68–75} while theoretical calculations predict near degeneracy of the other three with one or other of the experimentally measured states.^{76,77} In the following, the states are labeled according to the electron configuration from which they arise, in conjunction with the Hund’s case (c) notation. The $\dots(\sigma_g)^m(\pi_u)^p(\pi_g^*)^q(\sigma_u^*)^n$ notation for the electron configuration is abbreviated as $mpqn$,⁶⁷ while the Hund’s case (c) state labels Ω_i reflect the projection of the total electronic angular momentum quantum number (Ω) and the symmetry designation with respect to inversion ($i=g$ or u). In addition, the Hund’s case (a) orbital symmetry designation is given in parentheses. For example, the lowest excited electronic state of I_2 [see Fig. 1(a)], arising from the $\dots(\sigma_g)^2(\pi_u)^4(\pi_g^*)^3(\sigma_u^*)^1$ electron configuration, is the $2431 A' 2_u(^3\Pi)$ state.

Spin–orbit interaction mixes the electron configurations, making possible the transitions to six of the seven experimentally characterized states of I_2 .⁵⁹ The exception is the ground $2440 X 0_g^+(^1\Sigma^+)$ state, which is not accessible by a one-electron detachment transition from the $2432 A' 1/2_g(^2\Pi)$ state of I_2^- and is therefore not included in Fig. 1(c). The six solid curves shown in Fig. 1(c) correspond to the $2431 A' 2_u(^3\Pi)$,^{31,78} $2431 A 1_u(^3\Pi)$,^{73,79} $2431 B' 0_u^-(^3\Pi)$,^{69,78} $2431 B'' 1_u(^1\Pi)$,³⁰ $2341 a 1_g(^3\Pi)$,^{30,68,78} and $2422 a' 0_g^+(^3\Sigma^-)$ ^{68,74,78} electronic states, all of which are, in principle, accessible in the detachment of the $A' \text{I}_2^-$ state. The state potentials shown in Fig. 1(a) are calculated using the experimentally determined parameters, whenever possible. In some cases, extrapolation

into the long-range region is necessary, using parameters from the work of Saute and Aubert–Frecon.⁷⁸ For reference, Fig. 1(a) also shows a dashed line corresponding to the bracketed term in Eq. (2), calculated with the A' potential of the anion, allowing for its comparison to the relevant I_2 states.

For each of the six neutral potentials in Fig. 1(a), the $e\text{KE}(R)$ dependence from Eq. (2) was combined with the I_2^- dissociation trajectory $R(t)$, calculated according to Eq. (1). In this way, the semiclassical evolution of $e\text{KE}$ versus time is determined. To account for the experimental resolution, the result is convoluted with a 300-fs-wide time-broadening function, yielding a projected $e\text{KE}(t)$.

The resulting $e\text{KE}(t)$ “trajectories,” corresponding to the photodetachment to the six neutral states included in Fig. 1(c), are shown in Fig. 4(a) as dashed white lines overlaying the experimental contour plot. The original $e\text{KE}(t)$ curves were calculated to about 650 fs, corresponding to $R \approx 11 \text{ \AA}$. This approaches the limit of the range where the neutral potentials are known reliably. The corresponding curves in Fig. 4(a) terminate at a shorter delay on account of the temporal broadening function convoluted with the original trajectories. The solid black line in Fig. 4(a) represents a mean $e\text{KE}$ from each of the nine possible detachment channels: the six included in the above-noted calculation and the three experimentally uncharacterized neutral states. The mean is calculated assuming equal oscillator strengths for each of the six channels shown in Fig. 1(c), while weighting the a and a' states by factors of 2 and 3, respectively, to account for the contributions of the experimentally uncharacterized $2341 2_g(^3\Pi)$, $1441 0_u^-(^3\Sigma^+)$, and $2332 3_u(^3\Delta)$ states.¹⁰

At short pump–probe delays, the mean simulated curve deviates somewhat from the experimental time–energy plot in Fig. 4(a). There are many factors that may contribute to this discrepancy. First, although the simulations are based, wherever possible, on experimentally determined potentials, at short pump–probe delays many of the neutral states are accessed at the steep inner wall of the potential, above the dissociation limit, necessitating data extrapolation. Second, uncertainties in the experimentally determined potentials may give rise to discrepancies between the simulation and experimental data. For example, R_e for the A' state of I_2^- is reported as 6.2 \AA , but with an uncertainty of approximately 10%.¹⁰ Other possibilities include temporal uncertainties in the experimental measurements, the crude nature of the model, particularly the assumption that the oscillator strengths and Franck–Condon factors for all transitions are similar. This assumption is likely to be particularly important in the short-range region, where the neutral states are most divergent. The photon energy most closely matches the detachment via the higher-energy neutral states, which might be expected to increase the Franck–Condon factors to these states with the overall effect of reducing the average $e\text{KE}$.

Given the good agreement between the simulation and the experimental data from 300 fs and on, it is likely that the main sources of disagreement at shorter delays are uncertainties in the repulsive part of the neutral potentials. From the dissociation trajectory $R(t)$, $t=300 \text{ fs}$ corresponds to $R \approx 6.5 \text{ \AA}$. For $R > 6.5 \text{ \AA}$, the I_2 potentials are relatively invari-

ant with respect to R and any variations in the eKE, therefore, reflect mainly the changes in the anionic A' state potential. The simulation nicely predicts the experimentally observed shift to slightly higher eKE in this region, corresponding to the system moving out of the long-range shallow potential well.

B. Modeling IBr^- dissociation

As the electronic-state potentials for IBr^- were developed only recently,^{37,38} to our knowledge the present work is the first time-resolved dynamical test of these calculations. Similar to the procedure described in Sec. IV A, the IBr^- dissociation trajectories were propagated on a 1 fs time-grid, assuming a zero starting velocity. This being the first test of the newly calculated potentials, the choice of a starting point, R_0 , assumes greater importance and is discussed in the following.

Similar to the I_2^- case, the lowest-energy one-electron detachment from the A' state of IBr^- , arising from the $\dots(\sigma)^2(\pi)^4(\pi^*)^3(\sigma^*)^2$ electron configuration, leaves the neutral IBr molecule in an excited $\dots(\sigma)^2(\pi)^4(\pi^*)^3(\sigma^*)^1$, rather than the ground $\dots(\sigma)^2(\pi)^4(\pi^*)^4(\sigma^*)^0$ configuration. The potential energy curves corresponding to the IBr neutral states are not as extensively characterized as those of I_2 . Figure 1(d) shows the states that are likely to be relevant in detachment from the anion A' state at the probe photon energy used in the experiment.

The neutral A' state potential employed here is generated by the first-order Rydberg–Klein–Rees procedure using the RKR1 program of Le Roy⁷⁹ with the parameters from Radzykewycz *et al.*⁸⁰ The A, C , and Y states are calculated using the analytical forms of the potential curves determined by Ashfold and co-workers.⁸¹ In examining our time-resolved IBr^- data, we follow a similar treatment as in the case of I_2^- . However, given the incomplete data set of the neutral A' state and the “preliminary” nature of the Y state potential⁸¹ we limit ourselves to detachment via the A and C neutral state channels. These two states largely encompass the energy spread available in the final neutral states.

The $\text{eKE}(t)$ predicted using Eqs. (1) and (2) depends parametrically on R_0 . Based on the theoretical results,³⁷ the A' state of IBr^- is not classically accessible from the ground-state equilibrium geometry at the pump photon energy employed in the experiment. Therefore, we adopt three different approaches to choosing the value of R_0 .

The first approach is similar to the one described in Sec. IV A. It is to take the shortest I–Br bond length that energetically, in a classical sense, allows excitation to the A' state of the anion. This corresponds to $R_0=3.08$ Å. The trajectory launched from this internuclear distance, calculated according to Eq. (1), generates, using Eq. (2) and the convolution with a time-broadening function, one of the white dashed curves shown in Fig. 4(b). This $\text{eKE}(t)$ curve corresponds to the averaged contributions of the A and C neutral channels. Clearly, this trajectory underestimates the time required to reach the bottom of the well on the dissociation potential.

The ground-state bond strength of IBr^- relative to the $\text{I} + \text{Br}^-$ asymptotic limit was recently determined to be D_0

$=1.10\pm 0.04$ eV.³⁷ Examination of the theoretical X state potential shows that the calculation underestimates the well depth of the IBr^- ground state [see Fig. 1(d)].³⁷ This discrepancy can be corrected by scaling the calculated potential energy curves to reproduce the experimental result value of D_0 . Therefore, in our second approach to choosing R_0 , we take the point on the A' potential energy curve, which corresponds to the available energy relative to the experimentally determined $\text{I}^- + \text{Br}$ dissociation limit. The condition for determining R_0 is hence $V_{A'}(R_0) - V_{A'}(\infty) = h\nu - (D_0 + \Delta\text{EA})$, where $h\nu=1.59$ eV is the pump photon energy and $\Delta\text{EA}=0.305$ eV is the difference between the $\text{I}^- + \text{Br}$ and $\text{I} + \text{Br}^-$ asymptotic limits.⁶¹ Assuming the above experimental value of D_0 , this calculation yields $V_{A'}(R_0) - V_{A'}(\infty) = 0.185\pm 0.04$ eV. Comparing this available energy to the calculated $\text{IBr}^- A'$ potential energy curve^{37,38} yields $R_0 = 3.24\pm 0.05$ Å. The corresponding $\text{eKE}(t)$ “trajectory,” averaged over the contribution of the A and C neutral channels, is shown in Fig. 4(b) as the second dashed line. This trajectory is in better agreement with the experimental time–energy plot than the one for $R_0=3.08$ Å.

The third approach to selecting the starting point of the dissociation trajectory takes into account the uncertainty that exists in the relative energetics of the A' and X anion states. Since the calculations underestimate the ground-state dissociation energy, even larger error may be present in the calculated excited-state potential. Within the semiclassical framework, the energetic uncertainty can be accounted for by viewing R_0 as an adjustable rather than predetermined parameter. Hence, the third trajectory in Fig. 4(b), shown as a dashed white line, corresponds to $R_0=3.30$ Å, which (by inspection) yields the best agreement of the calculated $\text{eKE}(t)$ curve with the experiment.

C. Test of the $\text{IBr}^- A' 1/2(^2\Pi)$ state potential: Imaging the reaction coordinate

The agreement of the experimental data for I_2^- with the classical-trajectory calculations and the previous work on this system gives confidence in the new time-resolved results on IBr^- dissociation. The comparison of the latter results with the semiclassical predictions based on the recently calculated IBr^- potential energy curves provides the first dynamical test of these calculations. We observe good overall agreement of the theoretical predictions with the experimental data. The agreement allows us to conclude with confidence that the $A' 1/2(^2\Pi)$ potential of IBr^- calculated by Parson and co-workers^{37,38} adequately explains the observed time-resolved dynamics.

The experimental data in Fig. 4(b) reflect the time-dependent energy envelope of the dissociative wave packet launched by the pump laser pulse on the IBr^- excited-state potential. Every point along the time axis corresponds to a specific expectation value of R , making it possible to express the data in terms of R , the dissociation coordinate, rather than time. Strictly speaking, the wave packet is characterized by a spread in R values and, therefore, time cannot be unambiguously converted to R . Nonetheless, the classical trajectories $R(t)$ calculated in Sec. IV B allow for a formal

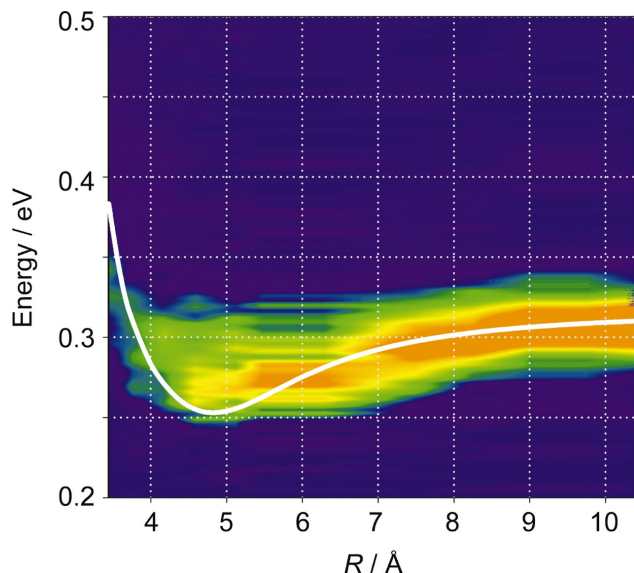


FIG. 5. (Color) An image of the $\text{IBr}^- A'$ potential based on the experimental data and semiclassical model described in the text. The corresponding theoretical potential energy curve (Refs. 37 and 38) is shown for comparison as a white line.

$(t, \text{eKE}) \rightarrow (R, \text{eKE})$ transformation on the experimental data set. While giving no new quantitative information that could not be obtained from the data in Fig. 4(b), this procedure provides an important insight into the evolving energy envelope in the reaction coordinate space.

According to Eq. (2), eKE reflects the difference between the anion A' and accessed neutral state potentials, corrected for the probe photon energy. Using an average of the neutral $C^1\Pi$ and $A^3\Pi$ potentials as a reference,⁸¹ the eKE coordinate in the experimental data set, already in the (R, eKE) space, can be transformed into the corresponding potential energy of the $A' 1/2(^2\Pi_{1/2})$ anion state, $V_{A'}$. The sequence of the two transforms, using, first, the trajectory $R(t)$, calculated via Eq. (1) with $R_0 = 3.30 \text{ \AA}$, and, second, the eKE(R) dependence from Eq. (2) with a mean of the A and C neutral potentials, was performed on the original experimental dataset in Fig. 4(b) to yield an overall $(t, \text{eKE}) \rightarrow (R, \text{eKE}) \rightarrow (R, V_{A'})$ transformation of the coordinates. The result is shown in Fig. 5.

This contour plot is, in essence, an experimental image of the dissociation potential as a function of the I–Br internuclear distance. The overall intensity variation with R signifies changes in the experimental signal strength and has no direct bearing on the shape of the potential. The spread in intensity along the energy axis reflects the experimental resolution, superimposed over the energy spread of the dissociative wave packet, as it propagates along the internuclear coordinate. For comparison, the white curve in Fig. 5 represents the calculated potential for the $\text{IBr}^- A' 1/2(^2\Pi_{1/2})$ state.^{37,38}

The agreement between the theoretical potential energy curve and the experimental image of the potential is remarkably good for $R \geq 6 \text{ \AA}$. The discrepancies observed at shorter bond lengths can be attributed to experimental and theoretical uncertainties. In particular, experimental time broadening leads to partial smearing of the $\sim 60 \text{ meV}$ deep well in the

image of the potential. To the contrary, no such broadening affects the calculated potential energy curve. In addition, the unavoidable time–energy uncertainty of the time-resolved measurement contributes to the distortion of the potential image. With these uncertainties in mind, the experimental “portrait” of the dissociation potential is in good agreement with theory.^{37,38}

V. SUMMARY AND FUTURE DIRECTIONS

Time-resolved anion photoelectron imaging was applied to study the photodissociation dynamics of IBr^- along the reaction coordinate. The results are discussed in comparison with photodissociation of I_2^- on the analogous electronic state, investigated under similar experimental conditions. Previous studies on the I_2^- anion^{8,10,56} were used as a reference for interpreting the IBr^- results.

The evolution of the energetics revealed in the time-resolved (780 nm pump, 390 nm probe) I_2^- and IBr^- photoelectron images was compared to the results of classical trajectory calculations on the respective A' excited-state anion potentials. The time-resolved photoelectron spectra were modeled assuming that a variety of neutral states were accessed in the probe-induced photodetachment. The experimental spectra for I_2^- obtained in the present work are in good agreement with the A' anion potential previously determined by Zanni *et al.* based on the measurements at a different (260 nm) probe wavelength.¹⁰ The experimental data and theoretical modeling of the IBr^- dissociation provide the first rigorous dynamical test of the recently calculated A' potential³⁷ for this system. In light of the good overall agreement of the experimental data with the theoretical predictions, the results are used to construct a snapshot of the IBr^- dissociation potential.

A future paper, currently in preparation, will discuss orbital symmetry effects in the photodissociation of the homonuclear and heteronuclear diatomic anions by examining in comparison the time-resolved photoelectron angular distributions in the photodissociation of I_2^- and IBr^- .

ACKNOWLEDGMENTS

We would like to acknowledge Mark A. Thompson and Professor Robert Parson for sending us the calculated IBr^- potential energy data prior to publication. We are thankful to Todd Sanford and Professor W. Carl Lineberger for enlightening discussions of IBr^- dissociation and sending us a preliminary draft as well as the final version of the manuscript³⁷ prior to its publication. Communications with Professor Martin T. Zanni regarding the X and A' state potentials of I_2^- are also gratefully acknowledged. The financial support for this work is provided by the National Science Foundation (Grant No. CHE-0134631), the Arnold and Mabel Beckman Foundation (Beckman Young Investigator Award), the David and Lucile Packard Foundation (Packard Fellowship for Science and Engineering), and the Camille and Henry Dreyfus Foundation (Camille Dreyfus Teacher-Scholar Award).

¹A. H. Zewail, J. Phys. Chem. **100**, 12701 (1996).

²A. H. Zewail, J. Phys. Chem. A **104**, 5660 (2000).

³M. T. Zanni, A. V. Davis, C. Frischkorn, M. Elhanine, and D. M. Neu-

- mark, J. Chem. Phys. **112**, 8847 (2000).
- ⁴M. T. Zanni, A. V. Davis, C. Frischkorn, M. Elhanine, and D. M. Neumark, J. Chem. Phys. **113**, 8854 (2000).
- ⁵D. M. Neumark, Annu. Rev. Phys. Chem. **52**, 255 (2001).
- ⁶A. Stolow, A. E. Bragg, and D. M. Neumark, Chem. Rev. (Washington, D.C.) **104**, 1719 (2004).
- ⁷K. M. Ervin and W. C. Lineberger, in *Advances in Gas Phase Ion Chemistry*, edited by N. G. Adams and L. M. Babcock (JAI, Greenwich, 1992), Vol. 1, p. 121.
- ⁸B. J. Greenblatt, M. T. Zanni, and D. M. Neumark, Chem. Phys. Lett. **258**, 523 (1996).
- ⁹M. T. Zanni, T. R. Taylor, B. J. Greenblatt, B. Soep, and D. M. Neumark, J. Chem. Phys. **107**, 7613 (1997).
- ¹⁰M. T. Zanni, V. S. Batista, B. J. Greenblatt, W. H. Miller, and D. M. Neumark, J. Chem. Phys. **110**, 3748 (1999).
- ¹¹D. W. Chandler and P. L. Houston, J. Chem. Phys. **87**, 1445 (1987).
- ¹²A. J. R. Heck and D. W. Chandler, Annu. Rev. Phys. Chem. **46**, 335 (1995).
- ¹³P. L. Houston, Acc. Chem. Res. **28**, 453 (1995).
- ¹⁴T. Seideman, J. Chem. Phys. **107**, 7859 (1997).
- ¹⁵T. Seideman, J. Chem. Phys. **113**, 1677 (2000).
- ¹⁶T. Seideman, Phys. Rev. A **64**, 042504 (2001).
- ¹⁷T. Seideman, Annu. Rev. Phys. Chem. **53**, 41 (2002).
- ¹⁸V. Blanchet, S. Lochbrunner, M. Schmitt, J. P. Shaffer, J. J. Larsen, M. Z. Zgierski, T. Seideman, and A. Stolow, Faraday Discuss. **115**, 33 (2000).
- ¹⁹V. Blanchet, M. Z. Zgierski, and A. Stolow, J. Chem. Phys. **114**, 1194 (2001).
- ²⁰M. Schmitt, S. Lochbrunner, J. P. Shaffer, J. J. Larsen, M. Z. Zgierski, and A. Stolow, J. Chem. Phys. **114**, 1206 (2001).
- ²¹S. Lochbrunner, J. J. Larsen, J. P. Shaffer, M. Schmitt, T. Schultz, J. G. Underwood, and A. Stolow, J. Electron Spectrosc. Relat. Phenom. **112**, 183 (2000).
- ²²S. Lochbrunner, T. Schultz, M. Schmitt, J. P. Shaffer, M. Z. Zgierski, and A. Stolow, J. Chem. Phys. **114**, 2519 (2001).
- ²³T. Suzuki, L. Wang, and H. Kohguchi, J. Chem. Phys. **111**, 4859 (1999).
- ²⁴L. Wang, H. Kohguchi, and T. Suzuki, Faraday Discuss. **113**, 37 (1999).
- ²⁵J. A. Davies, J. E. LeClaire, R. E. Continetti, and C. C. Hayden, J. Chem. Phys. **111**, 1 (1999).
- ²⁶A. E. Bragg, R. Wester, A. V. Davis, A. Kammrath, and D. M. Neumark, Chem. Phys. Lett. **376**, 767 (2003).
- ²⁷A. V. Davis, R. Wester, A. E. Bragg, and D. M. Neumark, J. Chem. Phys. **118**, 999 (2003).
- ²⁸B. Bagueard, J. C. Pinaré, F. Lépine, C. Bordas, and M. Broyer, Chem. Phys. Lett. **352**, 147 (2002).
- ²⁹B. Bagueard, J. C. Pinaré, C. Bordas, and M. Broyer, Phys. Rev. A **63**, 023204 (2001).
- ³⁰J. Tellinghuisen, J. Chem. Phys. **82**, 4012 (1985).
- ³¹X. N. Zheng, S. L. Fei, M. C. Heaven, and J. Tellinghuisen, J. Chem. Phys. **96**, 4877 (1992).
- ³²E. Surber and A. Sanov, J. Chem. Phys. **116**, 5921 (2002).
- ³³R. Mabbs, E. Surber, and A. Sanov, Analyst (Cambridge, U.K.) **128**, 765 (2003).
- ³⁴E. Surber, R. Mabbs, and A. Sanov, J. Phys. Chem. A **107**, 8215 (2003).
- ³⁵H. J. Deyerl, L. S. Alconcel, and R. E. Continetti, J. Phys. Chem. A **105**, 552 (2001).
- ³⁶R. Mabbs, K. Pichugin, E. Surber, and A. Sanov, J. Chem. Phys. **121**, 265 (2004).
- ³⁷T. Sanford, S.-Y. Han, M. A. Thompson, R. Parson, and W. C. Lineberger, J. Chem. Phys. **122**, 054307 (2005).
- ³⁸M. A. Thompson and R. Parson (private communication).
- ³⁹J. C. Alfano, Y. Kimura, P. K. Walhout, and P. F. Barbara, Chem. Phys. **175**, 147 (1993).
- ⁴⁰D. A. V. Kliner, J. C. Alfano, and P. F. Barbara, J. Chem. Phys. **98**, 5375 (1993).
- ⁴¹P. K. Walhout, J. C. Alfano, K. A. M. Thakur, and P. F. Barbara, J. Phys. Chem. **99**, 7568 (1995).
- ⁴²U. Banin and S. Ruhman, J. Chem. Phys. **98**, 4391 (1993).
- ⁴³E. Gershgoren, U. Banin, and S. Ruhman, J. Phys. Chem. A **102**, 9 (1998).
- ⁴⁴H. Yasumatsu, S. Koizumi, A. Terasaki, and T. Kondow, J. Chem. Phys. **105**, 9509 (1996).
- ⁴⁵H. Yasumatsu, A. Terasaki, and T. Kondow, J. Chem. Phys. **106**, 3806 (1997).
- ⁴⁶F. G. Amar and L. Perera, Z. Phys. D: At., Mol. Clusters **20**, 173 (1991).
- ⁴⁷B. J. Gertner, K. Ando, R. Bianco, and J. T. Hynes, Chem. Phys. **183**, 309 (1994).
- ⁴⁸R. Bianco and J. T. Hynes, J. Chem. Phys. **102**, 7864 (1995).
- ⁴⁹R. Bianco and J. T. Hynes, J. Chem. Phys. **102**, 7885 (1995).
- ⁵⁰I. Benjamin, P. F. Barbara, B. J. Gertner, and J. T. Hynes, J. Phys. Chem. **99**, 7557 (1995).
- ⁵¹D. Ray, N. E. Levinger, J. M. Papanikolas, and W. C. Lineberger, J. Chem. Phys. **91**, 6533 (1989).
- ⁵²J. M. Papanikolas, V. Vorsa, M. E. Nadal, P. J. Campagnola, H. K. Buchenau, and W. C. Lineberger, J. Chem. Phys. **99**, 8733 (1993).
- ⁵³S. Nandi, A. Sanov, N. Delaney, J. Faeder, R. Parson, and W. C. Lineberger, J. Phys. Chem. A **102**, 8827 (1998).
- ⁵⁴A. Sanov, S. Nandi, and W. C. Lineberger, J. Chem. Phys. **108**, 5155 (1998).
- ⁵⁵A. Sanov, T. Sanford, S. Nandi, and W. C. Lineberger, J. Chem. Phys. **111**, 664 (1999).
- ⁵⁶B. J. Greenblatt, M. T. Zanni, and D. M. Neumark, Science **276**, 1675 (1997).
- ⁵⁷M. T. Zanni (private communication).
- ⁵⁸J. Faeder, N. Delaney, P. E. Maslen, and R. Parson, Chem. Phys. Lett. **270**, 196 (1997).
- ⁵⁹J. Faeder and R. Parson, J. Chem. Phys. **108**, 3909 (1998).
- ⁶⁰P. E. Maslen, J. Faeder, and R. Parson, Chem. Phys. Lett. **263**, 63 (1996).
- ⁶¹*CRC Handbook of Chemistry and Physics*, 84 ed. (CRC Press, Boca Raton, FL, 2004).
- ⁶²M. A. Johnson and W. C. Lineberger, in *Techniques for the Study of Ion-Molecule Reactions*, edited by J. M. Farrar and W. H. Saunders (Wiley, New York, 1988), p. 591.
- ⁶³M. E. Nadal, P. D. Kleiber, and W. C. Lineberger, J. Chem. Phys. **105**, 504 (1996).
- ⁶⁴A. T. J. B. Eppink and D. H. Parker, Rev. Sci. Instrum. **68**, 3477 (1997).
- ⁶⁵W. C. Wiley and I. H. McLaren, Rev. Sci. Instrum. **26**, 1150 (1955).
- ⁶⁶V. Dribinski, A. Ossadtchi, V. A. Mandelshtam, and H. Reisler, Rev. Sci. Instrum. **73**, 2634 (2002).
- ⁶⁷R. S. Mulliken, J. Chem. Phys. **55**, 288 (1971).
- ⁶⁸S. Churassy, F. Martin, R. Bacis, J. Vergès, and R. W. Field, J. Chem. Phys. **75**, 4863 (1981).
- ⁶⁹K. S. Viswanathan and J. Tellinghuisen, J. Mol. Spectrosc. **101**, 285 (1983).
- ⁷⁰J. W. Tromp and R. J. Le Roy, J. Mol. Spectrosc. **109**, 352 (1985).
- ⁷¹J. Tellinghuisen, J. Chem. Phys. **58**, 2821 (1973).
- ⁷²J. Tellinghuisen, J. Chem. Phys. **118**, 3532 (2003).
- ⁷³D. R. T. Appadoo, R. J. Le Roy, P. F. Bernath, S. Gerstenkorn, P. Luc, J. Vergès, J. Sinzelle, J. Chevillard, and Y. D'Aignaux, J. Chem. Phys. **104**, 903 (1996).
- ⁷⁴K. P. Lawley, M. A. MacDonald, R. J. Donovan, and A. Kvaran, Chem. Phys. Lett. **92**, 322 (1982).
- ⁷⁵F. Martin, R. Bacis, S. Churassy, and J. Vergès, J. Mol. Spectrosc. **116**, 71 (1986).
- ⁷⁶C. Teichteil and M. Pelissier, Chem. Phys. **180**, 1 (1994).
- ⁷⁷W. A. de Jong, L. Visscher, and W. C. Nieuwpoort, J. Chem. Phys. **107**, 9046 (1997).
- ⁷⁸M. Saute and M. Aubert-Frécon, J. Chem. Phys. **77**, 5639 (1982).
- ⁷⁹R. J. Le Roy, RKR1 2.0: Report No. Chemical Physics Research Report CP-657R, 2004.
- ⁸⁰D. T. Radzykewycz, C. D. Littlejohn, M. B. Carter, J. O. Clevenger, J. H. Purvis, and J. Tellinghuisen, J. Mol. Spectrosc. **166**, 287 (1994).
- ⁸¹E. Wrede, S. Laubach, S. Schulenburg, A. Brown, E. R. Wouters, A. J. Orr-Ewing, and M. N. R. Ashfold, J. Chem. Phys. **114**, 2629 (2001).